Direct Carbonate Reduction on Sn Oxide Surface

Original
Direct Carbonate Reduction on Sn Oxide Surface / Wang, Jun; Chen, Lijuan; Huang, Lan; Chen, Tengfei; Zeng, Juqin; Wenbo Ju, And. - In: CHEMSUSCHEM. - ISSN 1864-5631. - 18:12(2025). [10.1002/cssc.202500364]

Publisher:
Wiley

Published
DOI:10.1002/cssc.202500364

ChemSusChem
Chemistry–Sustainability–Energy–Materials

Chemistry Europe
European Chemical Societies Publishing

Title: Direct Carbonate Reduction on Sn Oxide Surface

Authors: Jun Wang, Lijuan Chen, Lan Huang, Tengfei Chen, Juqin Zeng, and Wenbo Ju

To be cited as: *ChemSusChem* **2025**, e202500364

Link to VoR: https://doi.org/10.1002/cssc.202500364

WILEY-VCH

Direct Carbonate Reduction on Sn Oxide Surface

Jun Wang[1,#], *Lijuan Chen*[1,#], *Lan Huang*[2,3], *Tengfei Chen*[1], *Juqin Zeng*[2,3,]*, *Wenbo Ju*[1,]*

1. School of Physics and Optoelectronics, South China University of Technology, Guangzhou, Guangdong, 510640, China

2. Department of Applied Science and Technology (DISAT), Politecnico di Torino, Corso Duca degli Abruzzi 24, Turin,10129, Italy

3. Istituto Italiano di Tecnologia – IIT, Centre for Sustainable Future Technologies (CSFT), Via Livorno 60, Turin, 10144, Italy

[#] Jun Wang and Lijuan Chen contributed equally to this work.

Corresponding Author

Wenbo Ju (wjuphy@scut.edu.cn), Juqin Zeng (juqin.zeng@polito.it)

ABSTRACT

Direct reduction of carbonate (CO_3^{2-}) to value-added chemicals presents several advantages for integrating CO_2 capture from air with electrochemical conversion at near-unity efficiency. However, a critical challenge lies in effectively adsorbing CO_3^{2-} as a reactive intermediate for sequential reduction. Density functional theory calculations indicate that the presence of oxygen vacancies (V_O) on a SnO_2 surface significantly enhances its reactivity toward CO_3^{2-} adsorption, with the resulting adsorbed species (*CO_3) detectable by Raman spectroscopy. *Operando* electrochemical Raman spectra have confirmed the formation of *CO_3 on the partially reduced SnO_2-xV_O surface. Pulsed electrolysis has successfully converted CO_3^{2-} to CO at a constant flow rate in an electrolyzer featuring a gas diffusion electrode configuration. A reaction cycle, encompassing SnO_2 partial reduction, CO_3^{2-} adsorption and reduction, and SnO_2 regeneration, has been proposed as a viable approach for continuous direct CO_3^{2-} reduction.

KEYWORDS

carbonate reduction, Sn oxide, Raman spectroscopy, floating electrode, pulsed electrolysis

INTRODUCTION

Electrocatalytic carbon dioxide reduction reaction (CO_2RR) represents a promising approach to addressing global carbon emissions by converting CO_2 into value-added chemicals or fuels, effectively closing the carbon cycle [1]. Early research utilized bicarbonate (HCO_3^-) buffer solutions as electrolytes due to their ability to enhance CO_2 solubility and availability while ensuring compatibility with certain nonnoble electrocatalysts [2]. However, these neutral electrolytes suffer from limited ionic conductivity, hindering charge transport and reaction efficiency. Acidic and alkaline electrolytes offer higher ionic conductivity as alternatives for CO_2RR, yet acidic electrolytes face challenges such as competing hydrogen evolution reaction (HER), which reduces product selectivity [3], while alkaline environments lead to unintended CO_2 side reactions that form carbonate (CO_3^{2-}), contributing to carbon loss [4]. Moreover, the removal and recovery of CO_2 from product streams represents the most energy-intensive step in the downstream purification process [5]. Thus, suppressing the competing HER, preventing losses due to CO_3^{2-} formation, and simplifying the downstream purification process are crucial for the industrial application of CO_2RR.

Instead of reducing CO_2 from a gas stream, the electrochemical reduction of HCO_3^-/CO_3^{2-} presents several advantages for coupling CO_2 capture with conversion [6]. This approach eliminates the need for energy-intensive CO_2 recovery and compression steps, and has the potential for achieving near-unity conversion efficiency of captured CO_2 molecules [7]. In 2019, the membrane electrode assembly (MEA) system incorporating a bipolar membrane was introduced into HCO_3^- and CO_3^{2-} electrolyzers [8]. Berlinguette and colleagues [8a] used a N_2-saturated 3.0 M $KHCO_3$ solution as the feedstock for electrolysis, yielding CO with a Faradaic efficiency (FE) of 81% at 25 $mA{\cdot}cm^{-2}$. The Sargent group [8b] demonstrated CO_3^{2-} electrolysis, generating a pure syngas product stream at a current density of 150 $mA{\cdot}cm^{-2}$ and an energy efficiency of 35%. The bipolar membrane facilitates the generation of protons (H^+) and hydroxide (OH^-) ions through water dissociation [9], driving the HCO_3^- buffer system to produce CO_2 at the acidic interface, as evidenced by the observation of in situ CO_2 bubble formation [8a]. This concept has been adapted for various electrocatalysts, including Ag [10], Bi [11], Sn [12], and Cu [13], demonstrating the substantial influence of the chosen electrocatalyst on product selectivity. HCO_3^- electrolyzers offer higher product selectivity and energy efficiency compared to CO_3^{2-} electrolyzers, primarily due to the more straightforward conversion of HCO_3^- to CO_2. However, CO_3^{2-} as the feedstock has a significant advantage: CO_3^{2-} solutions can be obtained through direct air capture [6].

Adsorbed carbonate ($^*CO_3$) is a reactive intermediate involved in the electrochemical CO_2RR [14]. Ma et al. [15] experimentally identified that formate ($HCOO^-$) can be directly generated from the electroreduction of $Cu_2(CO_3)(OH)_2$ with Cu-CO_3^{2-} acting as the active intermediates. They then applied pulsed potentials to form Cu-CO_3^{2-} species from a K_2CO_3 solution on Cu, which were subsequently reduced to $HCOO^-$, demonstrating the feasibility of direct CO_3^{2-} reduction reaction (CO_3RR). The Bocarsly group [16] revealed that Sn oxides (SnO_x) are critical in the CO_2RR, as they interact with CO_2 to form surface-bound $^*CO_3$ species, which are reduced to $HCOO^-$.

Motivated by the existence of the Sn–CO_3 intermediate, we explored the direct CO_3RR on SnO_x surfaces. Density functional theory (DFT) calculations indicate that the presence of oxygen vacancies (V_O) on a SnO_2 surface significantly enhances its reactivity toward CO_3^{2-} adsorption, with the resulting adsorbed species ($*CO_3$) detectable by Raman spectroscopy. *Operando* electrochemical Raman spectra have confirmed the formation of $*CO_3$ on the partially reduced SnO_2-xV_O surface. Pulsed electrolysis has successfully converted CO_3^{2-} to CO. A reaction cycle, encompassing SnO_2 partial reduction, CO_3^{2-} adsorption and reduction, and SnO_2 regeneration, has been proposed as a viable approach for continuous direct CO_3^{2-} reduction.

RESULTS AND DISCUSSION

CO_3^{2-} adsorption

The CO_3^{2-} adsorption on the SnO_2 (110) surfaces, both with and without V_O, was simulated using density functional theory (DFT). SnO_2 adopts the rutile structure, where the ideal lattice features O atoms bonded to three Sn atoms, each coordinated by six O atoms [17]. The perfect SnO_2 (110) surface contains dangling O atoms (Figure S1a), whereas electrochemical reduction removes these dangling O atoms (SnO_2-xV_O), eventually eliminating them completely at SnO_2-$4V_O$ (Figure S1e). On the perfect SnO_2 surface, CO_3^{2-} interacts weakly, with an adsorption energy of only 1.75 eV, stabilizing through two Sn–O bonds (Figure 1a). In contrast, the presence of V_O significantly enhances reactivity toward CO_3^{2-} adsorption. A CO_3^{2-} anion adsorbs on the SnO_2-xV_O surface via three Sn–O bonds. When the number of V_O exceeds three in the model slab, the surface shifts from favoring proton (H^+) adsorption to favoring CO_3^{2-} adsorption (Figure 1b). Although HCO_3^{2-} and $HCOO^-$ weakly adsorb on the perfect SnO_2 surface, the increase in V_O does not notably enhance their adsorption energies, making them less active for adsorption compared to CO_3^{2-} (Figure 1c and S2). On the SnO_2-$4V_O$ surface, CO_3^{2-} is the most favored ion for adsorption among the five ions investigated (Figure S3).

A stable $*CO_3$ ensemble exhibits a range of vibrational features, including the twisting motion of two O atoms moving out of the trigonal $*CO_3$ plane and the rocking vibrations of O atoms around the central C atom, corresponding to computed Raman bands at 75.17 and 99.24 cm^{-1}, respectively (Figure 1d). Overall, the simulations indicate that a partially reduced SnO_2-xV_O surface significantly enhances the CO_3^{2-}

adsorption. The stable $*CO_3$ ensemble is expected to be experimentally probed in the low-frequency region of the Raman spectrum.

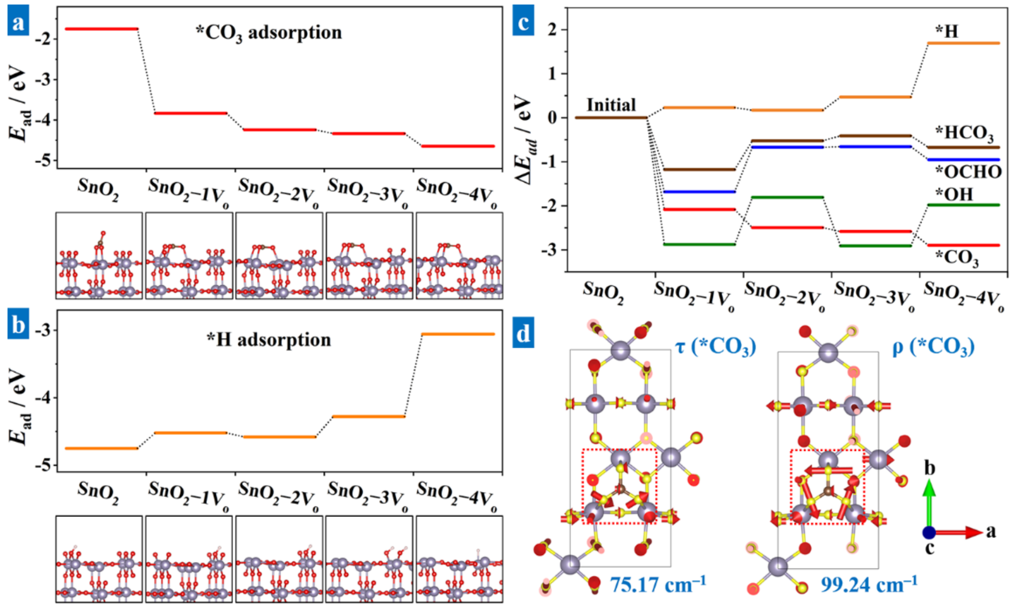

Figure 1 Adsorption energy of (a) $*CO_3$ and (b) $*H$ species on SnO_2 and SnO_2-xV_O surfaces ($x = 1$ to 4). (c) Change of adsorption energy of $*CO_3$, $*H$, $*OCHO$, $*HCO_3$, $*OH$ species on SnO_2-xV_O surfaces compared to SnO_2. (d) Raman-active vibrational modes of $*CO_3$ at frequencies of 75.17 and 99.24 cm^{-1}.

Detection of $*CO_3$

SnO_2 particles supported on a carbon paper act as the active species for electrochemical measurements in a typical spectro-electrochemical cell (Figure S4a to c). These particles exhibit three prominent Raman bands at 476, 643, and 782 cm^{-1} (Figure S4d), corresponding to the E_g, A_{1g}, and B_{2g} vibrational modes of SnO_2 crystals, respectively [18]. The first *operando* electrochemical Raman spectroscopy was conducted in a CO_2-saturated 0.5 M $KHCO_3$ solution (pH 7.3) (Figure 2a). The electrolyte was dynamically cycled over the electrode surface, ensuring a stable local pH. When SnO_2 particles are immersed in the electrolyte, the A_{1g} peak shows higher intensity compared to the E_g and B_{2g} peaks, making it a reliable indicator for detecting the presence of SnO_2 (Figure 2b). The cyclic voltammograms (CVs) of SnO_2 in the electrolyte show two reduction peaks at 0.06 and –0.38 V_{RHE} (vs. reversible hydrogen electrode) (Figure S5), corresponding to the sequential reduction of Sn^{4+} to Sn^{2+} and Sn^0, as indicated by Pourbaix analysis [19]. However, the intensity of the SnO_2 A_{1g} peak remains nearly constant above –0.40 V_{RHE}, but diminishes between –0.40 and –0.88 V_{RHE}, accompanied by the appearance of the E_g and A_{1g} vibrational features of SnO [20] (Figure 2b). Thus, SnO_2 appears to be only partially reduced due to kinetical hinderance [18, 21]. The surface may also expose a few metallic Sn layers, which are challenging to detect using state-of-the-art *operando* techniques [22]. The Raman intensity map reveals the direct transition of SnO_2 to SnO, consistent with the findings by Dutta et al. [18, 21] (Figure 2c). Notably, conventional *in situ* techniques inherently struggle to provide direct evidence of V_O, necessitating more advanced methods, such as electron paramagnetic resonance spectroscopy, to detect paramagnetic intermediates [23]. Logistic fitting curves, showing a decrease in SnO_2 intensity and an increase in SnO intensity, suggest that the phase transition occurs at –0.60 V_{RHE} (Figure 2d). In the presence of CO_2, a buffer system is established in the electrolyte, maintaining the pH near the pK_a of the $CO_2 \leftrightarrow HCO_3^-$ reversible reaction. The $*CO_3$ species are undetectable by Raman spectroscopy, likely due to the negligible CO_3^{2-} concentration at this pH.

Both CO_2RR and HER consume H^+ or produce OH^-, increasing the pH near the electrode surface, which is critical in determining the overall reaction dynamics [24]. If CO_2 is not continuously purged into the electrolyte, the buffering capacity of the HCO_3^- solution may become insufficient to maintain a stable pH. As the pH rises, the $HCO_3^- \leftrightarrow CO_3^{2-}$ equilibrium shifts, promoting CO_3^{2-} formation. The second *operando* electrochemical Raman spectroscopy was performed in an Ar-purged 0.5 M $KHCO_3$ solution (pH 8.1). Prior to recording the Raman spectra, potential cycling between 0.97 and –1.03 V_{RHE} was applied to adjust the electrochemical environment near the electrode surface (Figure S6). As the reactions involve the redox processes of SnO_x and the HER, the electrolyte pH increases to 8.9, with an even higher local pH expected (Figure 2e). The intensity of the SnO_2 A_{1g} peak remains nearly constant above 0.32 V_{RHE}, with no additional species detected in the Raman spectra across the range of 60 to 1100 cm^{-1} (Figure 2f). At 0.16 V_{RHE}, however, a broad band appears within the range of 60 to 120 cm^{-1}. As the potential is further swept to –0.16 V_{RHE}, this band resolves into two distinct peaks at 72 and 96 cm^{-1}, indicating the formation of $*CO_3$ on the partially reduced SnO_2-xV_O surface, referred to as $SnOCO_3$. The vibrational modes of $SnOCO_3$ vanish at –0.64 V_{RHE}, while the SnO E_g vibration emerges. The potential-dependent intensity map reveals the two-step reduction of SnO_2 to SnO, with $SnOCO_3$ acting as an intermediate state (Figure 2g). Logistic fitting of the intensity of the SnO_2 A_{1g} peak reveals two distinct transitions: a partial conversion of SnO_2 to $SnOCO_3$ at –0.01 V_{RHE}, followed by the complete reduction to SnO at approximately –0.57 V_{RHE} (Figure 2h). The potential for the phase transition from SnO_2 to SnO is consistent with the value measured in the CO_2-saturated 0.5 $KHCO_3$ solution, indicating that the reduction behavior is not significantly influenced by the electrolyte composition. The intensity of the $SnOCO_3$ peak reaches its maximum at –0.40 V_{RHE}, then diminishes rapidly as SnO_2 undergoes further reduction. The presence of CO_3^{2-}, resulting from the transition from HCO_3^- to CO_3^{2-} at a high local pH, promotes the formation of $*CO_3$ intermediates, as confirmed by the Raman spectra. However, the assumption that a high local pH arises from prior potential cycling remains speculative, as no experimental evidence currently supports this claim. Raman spectroscopy can distinguish between HCO_3^- and CO_3^{2-} through the C–OH stretching mode in HCO_3^- (1017 cm^{-1}) and the O–C–O symmetric stretching mode in CO_3^{2-} (1064 cm^{-1}) [25], but it fails to detect the

10.1002/cssc.202500364

transition from HCO_3^- to CO_3^{2-} using a typical spectro-electrochemical cell, due to the thick electrolyte layer in the light path.

The spectro-electrochemical cell was redesigned to accommodate to a floating electrode (Figure S7). The hydrophilic carbon paper floats on the electrolyte, with the electrolyte penetrating from the backside through the micropores, establishing an ultrathin electrolyte overlayer on the surface. Additionally, the floating electrode facilitates gas diffusion, forming a three-phase interface similar to that of a gas diffusion electrode (GDE) [26]. *Operando* electrochemical Raman spectroscopy was then conducted using an Ar-purged 0.5 M $KHCO_3$ solution (pH 8.1) (Figure 3a). The floating-electrode configuration enables direct observation of the transition from HCO_3^- to CO_3^{2-} during the negative potential sweep from –0.03 to –0.57 V_{RHE} (Figure 3b). The Raman band of CO_3^{2-}, initially negligible in the $KHCO_3$ solution, intensifies as the electrode potential drops below –0.21 V_{RHE}. CVs confirm that the HER does not occur above –0.62 V_{RHE} (Figure S6), ruling it out as a source of alkalization. Instead, the electroreduction of SnO_2 releases OH^-, raising the local pH and driving the

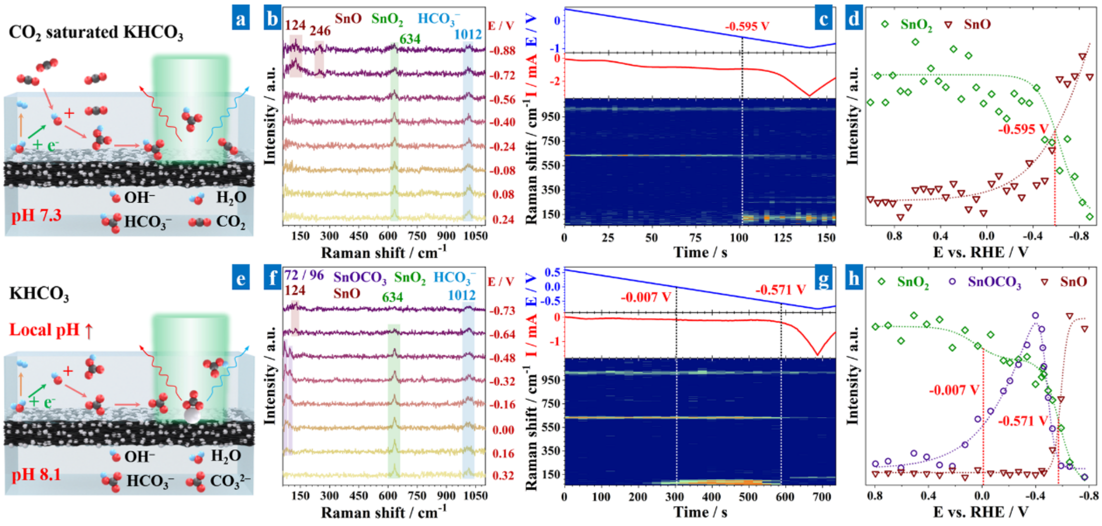

Figure 2 (a) Schematic diagram of *operando* electrochemical Raman spectroscopy conducted in a CO_2-saturated $KHCO_3$ solution at a stable pH of 7.3. (b) Raman spectra, (c) Raman intensity map, and (d) peak intensity analysis during a potential sweep. (e) Schematic diagram of *operando* electrochemical Raman spectroscopy conducted in an Ar-purged $KHCO_3$ solution at a pH higher than 8.1. (f) Raman spectra, (g) Raman intensity map, and (h) peak intensity analysis during a potential sweep.

transition from HCO_3^- to CO_3^{2-}. As the potential decreases further below –0.51 V_{RHE}, the Raman band of CO_3^{2-} becomes more prominent than that of HCO_3^- (Figure 3c). The $SnOCO_3$ formation at –0.64 V_{RHE} follows the generation of CO_3^{2-}, confirming that the presence of CO_3^{2-} is a prerequisite for $^*CO_3$ (Figure 3d). Both SnO_2 and $SnOCO_3$ persist at potentials as low as –0.91 V_{RHE}, seemingly contradicting previous experimental findings shown in Figure 2d and 2h. However, the electrode potential is referenced to the RHE after calculation using an electrolyte pH of 8.1. The significantly elevated local pH within the ultrathin electrolyte overlayer may result in an inaccurate estimation of the actual electrode potential, which is likely more positive.

Operando electrochemical Raman spectra were captured in an Ar-saturated 0.5 M K_2CO_3 solution (pH 12.1) (Figure 3e). A pH exceeding 12 is sufficiently high to drive the complete conversion of CO_2 and HCO_3^- into CO_3^{2-}, ensuring high CO_3^{2-} purity [27]. SnO_2 remains stable in the CO_3^{2-} environment at the OCP, but undergoes reduction at potentials more negative than 0.11 V_{RHE} (Figure S8). The Raman intensity of SnO_2 decreases at approximately –0.30 V_{RHE}, coinciding with the appearance of the $SnOCO_3$-related Raman bands (Figure 3f). The Raman intensity of $SnOCO_3$ is even more pronounced than that of SnO_2 in the potential range from –0.35 to –0.72 V_{RHE}, with a maximum at approximately –0.60 V_{RHE}, indicating the abundant formation of $^*CO_3$ on the surface (Figure 3g). Both SnO_2 and $SnOCO_3$ are simultaneously reduced at –0.72

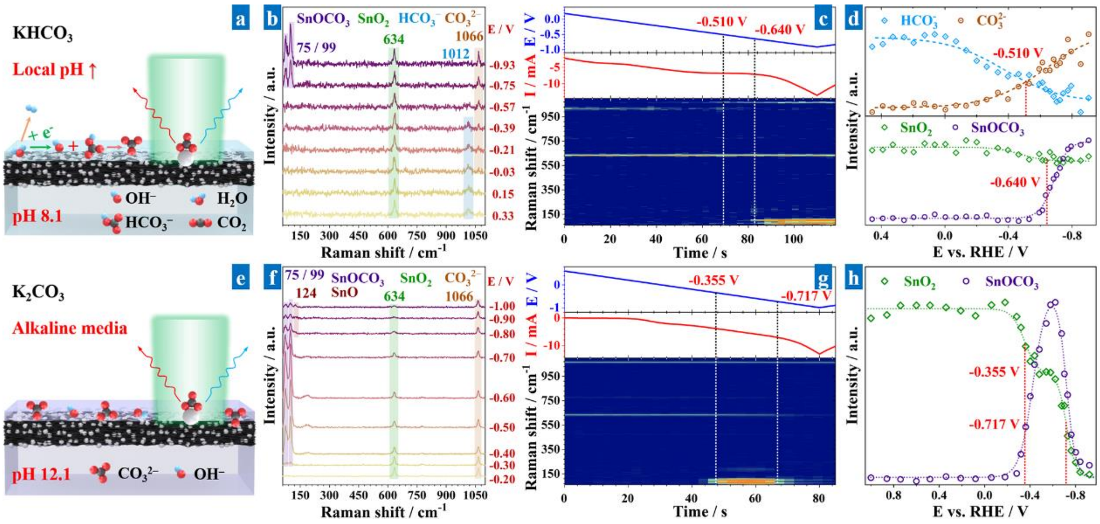

Figure 3 (a) Schematic diagram of *operando* electrochemical Raman spectroscopy conducted in an Ar-saturated KHCO$_3$ solution using a spectro-electrochemical cell with a floating electrode configuration. (b) Raman spectra, (c) Raman intensity map, and (d) peak intensity analysis during a potential sweep. (e) Schematic diagram of *operando* electrochemical Raman spectroscopy conducted in an Ar-saturated K$_2$CO$_3$ solution at a pH of 12.1. (f) Raman spectra, (g) Raman intensity map, and (h) peak intensity analysis during a potential sweep.

V_{RHE} (Figure 3h), exhibiting a reduction potential comparable to that observed in KHCO$_3$ solutions (Figure 2h). In general, CO_3^{2-} can adsorb onto a partially reduced SnO_2-xV_O surface, forming SnOCO$_3$, which can then be reduced to SnO at more negative potentials. Identifying the released carbon-containing species from SnOCO$_3$ is crucial to determining whether CO_3^{2-} undergoes reduction or remains unchanged. However, Raman spectroscopy, aside from detecting phase changes in electrocatalysts and transitions of Raman-active species in the electrolyte, does not provide information on reaction products, likely due to their relatively low concentration.

Direct CO_3^{2-} reduction

A CO_3^{2-} electrolyzer with a GDE configuration was used to characterize the reduction products (Figure 4a). The atmospheric conditions were adjusted by the gas flow. An anion exchange membrane (AEM) separated the counter electrode from the chamber housing the working and reference electrodes. SnO$_2$ particles were drop-cast onto a PTFE-treated carbon paper with a geometric area of 6.25 cm^2. Pulsed electrolysis, comprising three sequential steps, was applied to form $*CO_3$ at –0.70 V_{RHE}, reduce $*CO_3$ to final products at –1.00 V_{RHE}, and spontaneously regenerate SnO_2 surface at the OCP (Figure 4b). The potential of –0.70 V_{RHE} is selected for $*CO_3$ formation following a series of Raman analyses during chronoamperometry at potentials ranging from –0.64 to –0.74 V_{RHE}, as $*CO_3$ forms efficiently within 10 seconds and remains stable after prolonged holding at this potential (Figure S9). O_2 is required in the atmosphere, as SnO formed upon electroreduction of $SnOCO_3$ can spontaneously oxidize to SnO_2 at the OCP in the presence of O_2 (Figure S10a to c). In contrast, the SnO surface retains its reduced state for an extended period at the OCP in an Ar atmosphere, with only trace amounts of $SnOCO_3$ forming on the surface (Figure S10d to f). The intensity of SnO_2 remains minimal after 20 seconds.

A mixture of 80% Ar and 20% O_2 was flowed through the gas chamber during CO_3^{2-} electrolysis. Electrochemically produced CO diffuses into the chamber, reaching a steady concentration of approximately 550 ppm after 30 minutes (Figure 4c). $HCOO^-$, with a concentration of 83 ppm, has been detected in the electrolyte (Figure S11). The pulsed electrolysis generates CO as the primary product, which contrasts with the commonly reported high $HCOO^-$ selectivity of Sn-based electrocatalysts. Prior experimental studies have demonstrated that, at low overpotentials, oxidized Sn catalysts enhance CO selectivity during CO_2RR [16a, 28]. However, as the overpotential increases, CO selectivity declines, giving way to predominant $HCOO^-$ formation. This shift is likely attributable to variations in the oxidation state of the Sn catalysts and changes in activation energy that alter the reaction pathway [29].

H_2 is undetectable, indicating negligible HER. Although the reduction currents during the pulsed electrolysis approach values of –60 mA at –0.70 V_{RHE} and –150 mA at –1.00 V_{RHE} (Figure S12a), the production of CO and $HCOO^-$ contributes only 4.5% of the total transfer change, resulting in a low Faraday efficiency (FE) for CO_3RR. The remaining charge is consumed by the oxygen reduction reaction (ORR), which cannot be avoided in an O_2-containing atmosphere at such negative potentials.

Pulsed electrolysis was also performed in an Ar atmosphere. In the absence of O_2, the reduction current at –0.70 V_{RHE} approaches 0 mA (Figure S12b), indicating that neither the HER nor the $*CO_3$ formation occurs at this potential. However, at –1.00 V_{RHE}, the electrolysis exclusively generates H_2 with an average concentration of 1760 ppm (Figure 4d). Only trace amounts of CO are detectable at the beginning of the experiment, and the concentration of $HCOO^-$ in the electrolyte is 14 ppm (Figure S11). This experiment confirms the critical role of fully oxidized SnO_2 in initiating the reaction cycle of CO_3RR. O_2 facilitates the spontaneous oxidation of SnO to SnO_2 at the OCP, which subsequently promotes CO_3^{2-} adsorption on the partially reduced SnO_2-xV_O surface. In the absence of O_2, electrochemical oxidation provides an alternative approach to regenerate fully oxidized Sn species in the form of hydroxides rather than SnO_2 (Figure S13). The role of Sn hydroxides in CO_3RR needs requires further investigation.

The reaction mechanism for direct CO_3RR on the Sn oxide surface is summarized in Figure 4e. SnO_2 undergoes partial reduction, generating V_O that facilitate CO_3^{2-} adsorption. The intermediate $*CO_3$ can then be further reduced to CO or $HCOO^-$ at more negative potentials, eventually leaving the SnO surface. A spontaneous oxidation of SnO to SnO_2 in an O_2 atmosphere is required to initiate the reaction cycle.

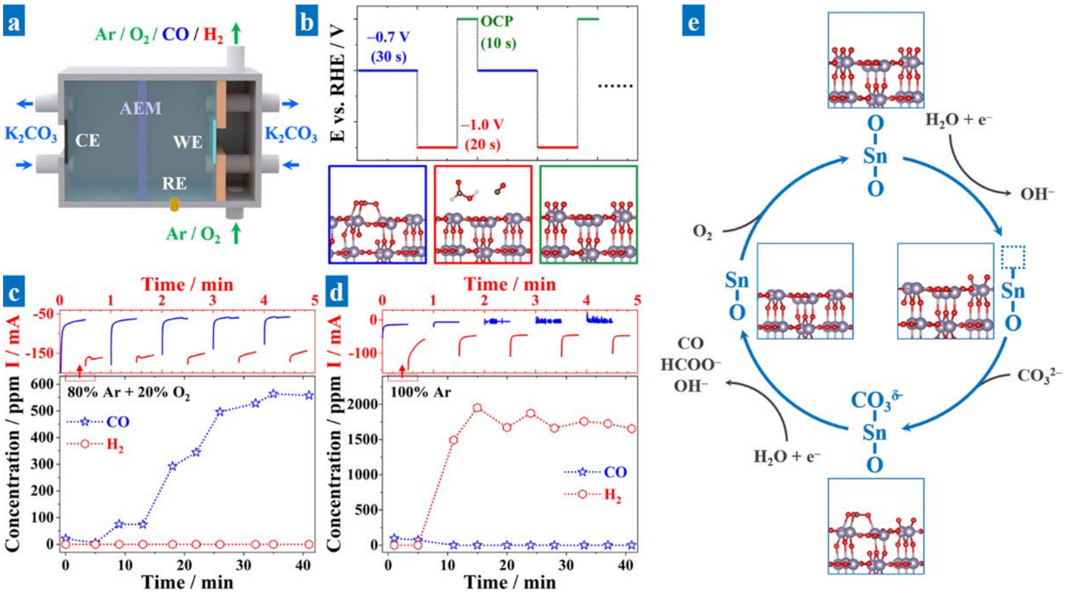

Figure 4 (a) Schematic diagram of a CO_3^{2-} electrolyzer with a GDE configuration. (b) Potential sequence in pulsed electrolysis, including steps for CO_3^{2-} adsorption at –0.70 V_{RHE}, $*CO_3$ reduction at –1.00 V_{RHE}, and SnO_2 regeneration at the OCP. Chronoamperograms in 5 minutes and concentrations of gaseous products during pulsed electrolysis in atmosphere of (c) 80% Ar and 20% O_2, and (d) 100% Ar. (e) Direct CO_3^{2-} reduction mechanism on Sn oxide surfaces.

CONLUSIONS

A partially reduced SnO_2-xV_O surface facilitates CO_3^{2-} adsorption to form $*CO_3$, which is subsequently reduced primarily to CO at more negative potentials. The SnO surface, formed after $*CO_3$ reduction, is no longer capable of adsorbing CO_3^{2-}. Therefore, the surface must be reoxidized to SnO_2 to initiate a new cycle of CO_3^{2-} adsorption and reduction. Pulsed electrolysis, comprising three sequential steps, has successfully converted CO_3^{2-} to CO at a constant flow rate in an electrolyzer with a GDE configuration. So far, O_2 is required in the atmosphere for SnO_2 regeneration of at the OCP, but its presence leads to energy consumption through the ORR, which lowers the Faraday efficiency for CO_3^{2-} reduction. Developing a strategy for SnO_2 regeneration that does not involve O_2 will be the most critical task in advancing a high-efficiency CO_3^{2-} electrolyzer. Nonetheless, direct reduction of CO_3^{2-} to value-added chemicals holds great promise for integrating CO_2 capture and conversion.

EXPERIMENTAL SECTION

Theoretical Calculation

Density functional theory (DFT) calculations were performed using the Vienna Ab initio Simulation Package (VASP) [30]. The generalized gradient approximation (GGA), in the form of the Perdew-Burke-Ernzerhof (PBE) functional [31], was employed to describe the electron exchange-correlation effects. Projector augmented wave (PAW) pseudopotentials were used to represent the ionic cores [32]. A cutoff energy of 450 eV and an atomic force convergence criterion of 0.02 eV/Å were applied.

The adsorption of various ions on SnO_2 and its partially reduced surface was computationally studies using models based on a SnO_2 (110) slab. The SnO_2 (110) surface was modeled using a (2 × 2) supercell with a four-layer periodic slab, where the two bottom layers were fixed. A Monkhorst-Pack k-mesh of 5 × 2 × 1 was used for Brillouin zone integrations in all systems. Additionally, the effect of van der Waals interactions between the four-layer periodic slab was incorporated using the empirical DFT-D3 correction scheme [33], as implemented in the Grimme method. A vacuum space of at least 15 Å was maintained between the slab and its periodic images in the vertical direction. More detailed information is provided in the Supporting Information.

Operando Electrochemical Raman spectroscopy

SnO_2 particles were drop-cast onto carbon paper (CP). SnO_2@CP electrodes (1.5 × 1.5 cm^2) were assembled into a typical spectro-electrochemical cell (K008, Ida) with a three-electrode configuration. The counter electrode was a Pt mesh (2 × 1 cm^2, wire diameter of 0.1 mm). The reference electrode was Ag/AgCl in a saturated KCl solution. The working electrode was fully immersed in the electrolyte, with a liquid gap of approximately 2.0 mm from the quartz window. SnO_2@CP electrodes (2.5 × 2.5 cm^2) were used as the working electrode in a redesigned spectro-electrochemical cell (Figure S7). The backside of the electrode was in contact with the upper layer of the electrolyte, allowing the electrolyte to penetrate through the micropores and form an ultrathin electrolyte overlayer on the surface. The frontside of the electrode was exposed to a gas chamber, with a gap of less than 5.0 mm from the quartz window. The counter electrode was a Pt mesh (2.5 × 2.5 cm^2, wire diameter of 0.1 mm). The reference electrode was Ag/AgCl in a saturated KCl solution. The liquid chamber for working electrode was separated from that for the counter electrode by an anion exchange membrane. More detailed information is provided in the Supporting Information.

Pulsed electrolysis

Pulsed electrolysis was conducted using a three-compartment electrolysis cell with a GDE configuration. SnO_2@CP electrodes (2.5 × 2.5 cm^2) were used as the working electrode. An Ar-saturated 0.5 M K_2CO_3 solution (pH = 12.1) was introduced into both the cathode and anode chambers, which were separated by an anion exchange membrane (Sustainion® X37-50 Grade RT). A miniature Ag/AgCl reference electrode was placed in the cathode chamber, while a Pt sheet (2.5 × 2.5 cm^2) was used as the counter electrode in the anode chamber. During the reaction, gas was passed over the GDE at a flow rate of 25 $mL \cdot min^{-1}$. The atmosphere in the gas chamber could be adjusted to either pure Ar or an Ar–O_2 mixture. Gaseous products were analyzed online using a micro gas chromatograph (μGC, Fusion, INFICON). Liquid products were identified and quantified using a high-performance liquid chromatography (HPLC, Thermo Scientific, Ultimate 3000). More detailed information is provided in the Supporting Information.

ACKNOWLEDGEMENTS

W.J. are grateful for the financial support from the Introduces Innovative and Entrepreneurial Team Project of Guangdong Province (No. 2021ZT09Z109), and the Basic and Applied Basic Research Foundation of Guangdong Province (No. 2024A1515012342). L.H. has received funding from the EU's Horizon 2021 programme under the Marie Skłodowska-Curie Doctoral Networks (MSCA-DN) (Grant agreement No 101072830). J.Z. was funded through the National Recovery and Resilience Plan (NRRP) of Italian Ministry of Research (Project code: IR0000027, CUP: B33C22000710006, Project title: iENTRANCE).

Electronic Supplementary Material

Supplementary material is available in the online version.

References

[1] aS. C. Peter, *ACS Energy Letters* **2018**, *3*, 1557-1561; bP. De Luna, C. Hahn, D. Higgins, S. A. Jaffer, T. F. Jaramillo, E. H. Sargent, *Science* **2019**, *364*, eaav3506.

[2] aG. Marcandalli, M. C. O. Monteiro, A. Goyal, M. T. M. Koper, *Accounts of Chemical Research* **2022**, *55*, 1900-1911; bM. Moura de Salles Pupo, R. Kortlever, *ChemPhysChem* **2019**, *20*, 2926-2935.

[3] Z. Yao, X. He, R. Lin, *Electrochemical Energy Reviews* **2024**, *7*, 8.

[4] aC. Chen, Y. Li, P. Yang, *Joule* **2021**, *5*, 737-742; bT. Zhang, J. Zhou, T. Luo, J.-Q. Lu, Z. Li, X. Weng, F. Yang, *Chemistry – A European Journal* **2023**, *29*, e202301455.

[5] T. Alerte, J. P. Edwards, C. M. Gabardo, C. P. O'Brien, A. Gaona, J. Wicks, A. Obradović, A. Sarkar, S. A. Jaffer, H. L. MacLean, D. Sinton, E. H. Sargent, *ACS Energy Letters* **2021**, *6*, 4405-4412.

[6] T. Li, M. Shao, *EES Catalysis* **2024**, *2*, 564-572.

[7] A. J. Welch, E. Dunn, J. S. DuChene, H. A. Atwater, *ACS Energy Letters* **2020**, *5*, 940-945.

[8] aT. Li, E. W. Lees, M. Goldman, D. A. Salvatore, D. M. Weekes, C. P. Berlinguette, *Joule* **2019**, *3*, 1487-1497; bY. C. Li, G. Lee, T. Yuan, Y. Wang, D.-H. Nam, Z. Wang, F. P. García de Arquer, Y. Lum, C.-T. Dinh, O. Voznyy, E. H. Sargent, *ACS Energy Letters* **2019**, *4*, 1427-1431.

[9] S. Z. Oener, M. J. Foster, S. W. Boettcher, *Science* **2020**, *369*, 1099-1103.

[10] aE. W. Lees, M. Goldman, A. G. Fink, D. J. Dvorak, D. A. Salvatore, Z. Zhang, N. W. X. Loo, C. P. Berlinguette, *ACS Energy Letters* **2020**, *5*, 2165-2173; bC. Larrea, D. Torres, J. R. Avilés-Moreno, P. Ocón, *Journal of CO2 Utilization* **2022**, *57*, 101878; cZ. Zhang, E. W. Lees, F. Habibzadeh, D. A. Salvatore, S. Ren, G. L. Simpson, D. G. Wheeler, A. Liu, C. P. Berlinguette, *Energy & Environmental Science* **2022**, *15*, 705-713.

[11] T. Li, E. W. Lees, Z. Zhang, C. P. Berlinguette, *ACS Energy Letters* **2020**, *5*, 2624-2630.

[12] O. Gutierrez-Sanchez, B. de Mot, M. Bulut, D. Pant, T. Breugelmans, *ACS Applied Materials & Interfaces* **2022**, *14*, 30760-30771.

[13] E. W. Lees, A. Liu, J. C. Bui, S. Ren, A. Z. Weber, C. P. Berlinguette, *ACS Energy Letters* **2022**, *7*, 1712-1718.

[14] aI. Zelocualtecatl Montiel, A. Dutta, K. Kiran, A. Rieder, A. Iarchuk, S. Vesztergom, M. Mirolo, I. Martens, J. Drnec, P. Broekmann, *ACS Catalysis* **2022**, *12*, 10872-10886; bY. Katayama, F. Nattino, L. Giordano, J. Hwang, R. R. Rao, O. Andreussi, N. Marzari, Y. Shao-Horn, *The Journal of Physical Chemistry C* **2018**, *123*, 5951-5963; cS. Zhu, B. Jiang, W. B. Cai, M. Shao, *Journal of the American Chemical Society* **2017**, *139*, 15664-15667.

[15] H. Ma, E. Ibáñez-Alé, R. Ganganahalli, J. Pérez-Ramírez, N. López, B. S. Yeo, *Journal of the American Chemical Society* **2023**, *145*, 24707-24716.

[16] aM. F. Baruch, J. E. Pander, J. L. White, A. B. Bocarsly, *ACS Catalysis* **2015**, *5*, 3148-3156; bJ. E. Pander, M. F. Baruch, A. B. Bocarsly, *ACS Catalysis* **2016**, *6*, 7824-7833.

[17] R. Gilani, S. U. Rehman, F. K. Butt, B. Ul Haq, F. Aleem, *Silicon* **2018**, *10*, 2317-2328.

[18] A. Dutta, A. Kuzume, M. Rahaman, S. Vesztergom, P. Broekmann, *ACS Catalysis* **2015**, *5*, 7498-7502.

[19] N. Takeno, National Institute of Advanced Industrial Science and Technology, **2005**.

[20] Y. Q. Guo, R. Q. Tan, X. Li, J. H. Zhao, Z. L. Luo, C. Gao, W. J. Song, *CrystEngComm* **2011**,

13, 5677-5680.

[21] A. Dutta, A. Kuzume, V. Kaliginedi, M. Rahaman, I. Sinev, M. Ahmadi, B. Roldán Cuenya, S. Vesztergom, P. Broekmann, *Nano Energy* **2018**, *53*, 828-840.

[22] C. Salvini, M. Re Fiorentin, F. Risplendi, F. Raffone, G. Cicero, *The Journal of Physical Chemistry C* **2022**, *126*, 14441-14447.

[23] M. Seif-Eddine, S. J. Cobb, Y. Dang, K. Abdiaziz, M. A. Bajada, E. Reisner, M. M. Roessler, *Nature Chemistry* **2024**, *16*, 1015-1023.

[24] M. C. O. Monteiro, A. Mirabal, L. Jacobse, K. Doblhoff-Dier, S. C. Barton, M. T. M. Koper, *JACS Au* **2021**, *1*, 1915-1924.

[25] J. D. Frantz, *Chemical Geology* **1998**, *152*, 211-225.

[26] S. Martens, L. Asen, G. Ercolano, F. Dionigi, C. Zalitis, A. Hawkins, A. Martinez Bonastre, L. Seidl, A. C. Knoll, J. Sharman, P. Strasser, D. Jones, O. Schneider, *Journal of Power Sources* **2018**, *392*, 274-284.

[27] H. Rho, Y.-g. Lee, J. Cho, Y. C. Woo, K. Chon, *Science of The Total Environment* **2023**, *903*, 166127.

[28] Y. Chen, M. W. Kanan, *Journal of the American Chemical Society* **2012**, *134*, 1986-1989.

[29] T. N. Whittaker, Y. Fishler, J. M. Clary, P. Brimley, A. Holewinski, C. B. Musgrave, C. A. Farberow, W. A. Smith, D. Vigil-Fowler, *ACS Catal* **2024**, *14*, 8353-8365.

[30] aG. Kresse, J. Hafner, *Physical Review B* **1993**, *47*, 558-561; bG. Kresse, J. Hafner, *Physical Review B* **1994**, *49*, 14251-14269; cG. Kresse, J. Furthmüller, *Computational Materials Science* **1996**, *6*, 15-50.

[31] aB. Hammer, L. B. Hansen, J. K. Nørskov, *Physical Review B* **1999**, *59*, 7413-7421; bJ. P. Perdew, K. Burke, M. Ernzerhof, *Physical Review Letters* **1996**, *77*, 3865-3868.

[32] aG. Kresse, J. Furthmüller, *Physical Review B* **1996**, *54*, 11169-11186; bP. E. Blöchl, *Physical Review B* **1994**, *50*, 17953-17979.

[33] S. Grimme, J. Antony, S. Ehrlich, H. Krieg, *The Journal of Chemical Physics* **2010**, *132*, 154104.